Optimizing vehicle aerodynamics through the synergistic application of Design of Experiments (DoE) and Computational Fluid Dynamics (CFD)

Yi Lu

High School Affiliated to Renmin University of China

luyi_albert@163.com

Abstract. The aerodynamic design of cars not only creates aesthetic and diverse car shapes, but also ensures their safety and fuel economy. According to Mustafa Cakir's research[1], approximately 11% of the fuel consumption of a car traveling at high speeds is used to counteract air resistance. However, with the increasing severity of global warming, emissions standards for automobile exhaust are becoming increasingly stringent. Considering that gasoline vehicles still dominate the household car market, optimizing the aerodynamic design of automobiles is imperative. This work analyzes and optimizes the aerodynamic design of automobiles through the synergistic application of Design of Experiments (DoE) and Computational Fluid Dynamics (CFD). Before conducting experiments, the article first introduces and derives the basic control equations of computational fluid dynamics, namely the continuity equation and Navier-Stokes equation, and describes how they are used in experiments. Then, the article briefly introduces the drag coefficients of automobiles, which are important theoretical basis for subsequent aerodynamic design optimization in this article. In the experimental part, this study focuses on the influence of four important design parameters: angle of the front window $\alpha(^\circ)$, angle of the hood $\beta(^\circ)$, angle of the back window $\theta(^\circ)$, and length of the trunk $L_t(\mathrm{mm})$. Using Solidworks 3D modeling software, the article simulates these design parameters and prepares for CFD numerical simulation by geometry, setting computational domain, boundary conditions, and objective functions, and generating mesh. Based on the DoE and numerical simulation results, the article ultimately selects a front window angle of 30°, a hood angle of 2.5°, a back window of 90°, and $L_t = 0\ \mathrm{mm}$ as the optimized design. Compared with the basic model, the optimized model reduces the drag coefficient by about 28%. The conclusion of this study provides ideas and theoretical basis for the aerodynamic optimization design of new generation automobiles with the incorporation of DoE. However, the design parameters of automobiles are countless, and in the future, this article will strive to research and simulate more diverse automobile designs and analyze their aerodynamic performance to explore more optimized designs.

Keywords: Aerodynamic Analysis, Automotive Design, 3-D Modeling, Computational Fluid Dynamics, Design of Experiment, Drag Coefficient, Flow Trajectories.

1. Introduction

As the road networks expanded and vehicle speeds increased, the significance of its aerodynamic design grew exponentially. Automotive aerodynamics, an intricate branch intimately connected with fluid mechanics, delves into the interaction between vehicles and the surrounding air, scrutinizing both external and internal airflow dynamics [2]. The ramifications of aerodynamic design extend beyond performance enhancements, exerting a profound influence on the outward appearance and aesthetic facets of automobiles.

More importantly, automotive aerodynamics plays a pivotal role in addressing vehicle exhaust emissions and is intrinsically linked to environmental concerns. In the face of escalating environmental challenges, there is a discernible shift towards more stringent emission standards for automobiles. To meet these emission standards, the efficient conversion of engine combustion energy into vehicle kinetic energy becomes paramount, underscoring the significance of aerodynamics in automotive design. Cakir's study [1] illustrates the fuel consumption of a vehicle at high speeds, with a substantial 11% of fuel energy dedicated to overcoming air resistance. This amount of energy expenditure at elevated speeds accentuates the pivotal role of aerodynamic design in the automotive

landscape. To perform further quantitative study over the air resistance of automobiles, Huang, Du, et al. [3,4] stated that aerodynamic drag N_d is proportional to the cube of the vehicle's velocity V, and the rolling friction N_R is directly proportional to the velocity. When the vehicle reaches $65\ \mathrm{km/h}$, the power N_e required for overcoming aerodynamic drag N_d begins to be greater than the power required for overcoming rolling friction N_R, which elicits the great significance to reduce aerodynamic drag for vehicles at high speeds.

The research methodologies in automobile aerodynamics, akin to those employed in various other realms of physics, are typically categorized into three principal domains: theory, computation, and experimentation [5]. Notably, the realm of Computational Fluid Dynamics (CFD) has experienced rapid advancement in recent years, evolving into a research methodology of equal importance alongside theoretical analysis and empirical investigations [3]. CFD primarily addresses fluid dynamics concerns through meticulous numerical analysis and intricate data structures, fostering reciprocal interactions with both theory and experimentation. This synergy fuels the continuous evolution and progress of automotive aerodynamics.

The field of automotive aerodynamics has garnered significant attention from researchers, yielding valuable insights. For instance, Qu et al. [6] employed computational fluid dynamics to design an orthogonal optimization test for rear structures. Their findings highlighted that comprehensive rear structure optimization could reduce the aerodynamic drag coefficient by a noteworthy 14.4%, effectively mitigating wake separation and tail vortex drag while enhancing wake dynamics. Mustafa Cakir [1] of Santa Clara University also harnessed computational fluid dynamics to investigate the impact of tail fins and airflow deflectors on household vehicle aerodynamics. Numerical simulations revealed that deflectors effectively curtailed air resistance by 17% and lift by 7% at high speeds. Wu [7], using the lattice Boltzmann algorithm as the foundational theory, conducted numerical simulations on the MIRA fastback model. Implementing active blowing or suction at six pivotal locations affecting aerodynamic drag coefficients, the study concluded that the active drag reduction method reduced air resistance by approximately 16.3%. Li [8] leveraged computational fluid dynamics simulation technology to study three driving conditions - trailing, crosswind, and overtaking - yielding valuable safety recommendations. Additionally, Mr. Li introduced rear enhancements like tail wings and ducktails, enhancing driving stability albeit at a slight cost to fuel economy. In a different domain, Reddy et al. [9] employed CFD numerical methods and FLUENT software to calculate the optimal attack angle for Formula One racing car (F1) front wings. Their research pinpointed that a 4-degree position yielded the minimum lift coefficient, thereby maximizing the ratio of lift coefficient to drag coefficient.

The aforementioned studies conducted both domestically and internationally serve as invaluable benchmarks for our research endeavor. Perusing the literature reveals the maturity and extensive practical applications of computational fluid dynamics (CFD). This versatile tool proves instrumental in enhancing the aerodynamic characteristics of everyday family vehicles and refining the intricate design intricacies of high-performance formula cars. It is crucial to acknowledge, however, that optimizing vehicle aerodynamics via CFD remains a time-consuming task, primarily due to the multitude of geometric parameters inherent in vehicle design. Therefore, in the present work, we performed the optimization of vehicle aerodynamics through the synergistic application of Design of Experiments (DoE) and Computational Fluid Dynamics (CFD).

This paper is structured as follows: Section 2 outlines the research methodology, encompassing the governing equations of Computational Fluid Dynamics (CFD), geometric considerations, computational domain, boundary conditions, mesh generation, and descriptions of CAD/CFD software tools. In Section 3, we introduce the Design of Experiment (DoE) approach, elaborating on its principles and implementation, as well as its application in our current study. Section 4 provides an in-depth examination of the results and engages in a thorough discussion based on the outcomes of the DoE and our analysis of vehicle aerodynamics. Finally, the paper concludes by summarizing our current findings and outlining potential avenues for future research.

2. Research Methods

This section first describes the governing equations of fluid mechanics, and then gives details on the numerical formulations of CFD used in the present work.

2.1. Governing Equations of CFD

2.1.1. Continuity equation (mass conservation)

The mass conservation states that for an arbitrary control volume, the net rate of mass increase within the volume is equal to the net mass flux into the volume. For example, in the infinitesimal control volume as shown in Figure 1, the rate of mass increase is $\frac{\partial(\rho \mathrm{d}x\ \mathrm{d}y\ \mathrm{d}z)}{\partial t}$. The net mass flux into the volume in x direction is the inflow rate minus the outflow rate, i.e.,

$$\rho v_x\ \mathrm{d}y\ \mathrm{d}z - (\rho v_x\ \mathrm{d}y\ \mathrm{d}z) + \frac{\partial(\rho v_x\ \mathrm{d}y\ \mathrm{d}z)}{\partial x}\ \mathrm{d}x = -\frac{\partial(\rho v_x)}{\partial x}\ \mathrm{d}x\ \mathrm{d}y\ \mathrm{d}z \tag{1}$$

And similarly, the net mass flux into the volume in y and z directions are

$$-\frac{\partial(\rho v_y)}{\partial y}\ \mathrm{d}x\ \mathrm{d}y\ \mathrm{d}z \tag{2}$$

$$-\frac{\partial(\rho v_z)}{\partial z}\ \mathrm{d}x\ \mathrm{d}y\ \mathrm{d}z \tag{3}$$

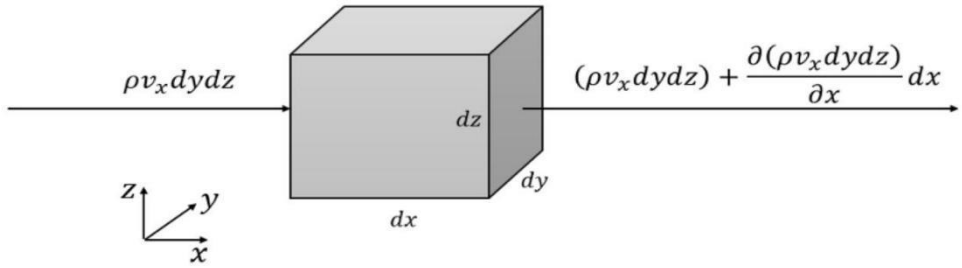


Figure 1: Taking x direction as an example showing mass conservation in the infinitesimal control volume

Summing the net mass fluxes into the volume in three directions (i.e, Equation 2.1, 2.2 and 2.3) introduces the total net mass fluxes, which equals to the rate of mass increase in the control volume, i.e,

$$-\frac{\partial(\rho v_x)}{\partial x}\ \mathrm{d}x\ \mathrm{d}y\ \mathrm{d}z - \frac{\partial(\rho v_y)}{\partial y}\ \mathrm{d}x\ \mathrm{d}y\ \mathrm{d}z - \frac{\partial(\rho v_z)}{\partial z}\ \mathrm{d}x\ \mathrm{d}y\ \mathrm{d}z = \frac{\partial \rho}{\partial t}\ \mathrm{d}x\ \mathrm{d}y\ \mathrm{d}z \tag{4}$$

by removing the term $\mathrm{d}x\ \mathrm{d}y\ \mathrm{d}z$, it comes,

$$-\left[\frac{\partial(\rho v_x)}{\partial x} + \frac{\partial(\rho v_y)}{\partial y} + \frac{\partial(\rho v_z)}{\partial z}\right] = \frac{\partial \rho}{\partial t} \tag{5}$$

For the general incompressible fluid flow, which is the case of my study, the density of the fluid is a constant value, i.e., $\rho =$ const which means the rate of mass increase $\frac{\partial \rho}{\partial t} = 0$, thus that the mass conservation can be expressed as,

$$\frac{\partial v_x}{\partial x} + \frac{\partial v_y}{\partial y} + \frac{\partial v_z}{\partial z} = 0 \tag{6}$$

2.1.2. Navier-Stokes equations (momentum conservation)

The law of momentum conservation, which is namely a stretch of the Newton's 2nd Law $F = ma$, can be deduced by expanding the equation of continuity along with the Newton's 2nd law. As this is a vector relation, it can be separated into forces on each of the three dimensions. In general, the forces that anticipate, including viscosity, pressure and gravity, can be demonstrated in the following equations in three directions $(x - 7, y - 8,\ z - 9)$:

$$\rho\left(\frac{\partial v_x}{\partial t}+v_x\frac{\partial v_x}{\partial x}+v_y\frac{\partial v_x}{\partial y}+v_z\frac{\partial v_x}{\partial z}\right)=\mu\left[\frac{\partial^2 v_x}{\partial x^2}+\frac{\partial^2 v_x}{\partial y^2}+\frac{\partial^2 v_x}{\partial z^2}\right]-\frac{\partial p}{\partial x} \tag{7}$$

$$\rho\left(\frac{\partial v_y}{\partial t}+v_x\frac{\partial v_y}{\partial x}+v_y\frac{\partial v_y}{\partial y}+v_z\frac{\partial v_y}{\partial z}\right)=\mu\left[\frac{\partial^2 v_y}{\partial x^2}+\frac{\partial^2 v_y}{\partial y^2}+\frac{\partial^2 v_y}{\partial z^2}\right]-\frac{\partial p}{\partial y}+\rho g_y \tag{8}$$

$$\rho\left(\frac{\partial v_z}{\partial t}+v_x\frac{\partial v_z}{\partial x}+v_y\frac{\partial v_z}{\partial y}+v_z\frac{\partial v_z}{\partial z}\right)=\mu\left[\frac{\partial^2 v_z}{\partial x^2}+\frac{\partial^2 v_z}{\partial y^2}+\frac{\partial^2 v_z}{\partial z^2}\right]-\frac{\partial p}{\partial z} \tag{9}$$

These equations are called the Navier-Stokes equations, which named after French physicist Claude-Louis Navier and Anglo-Irish physicist George Gabriel Stokes. Combining the Navier-Stokes equations with the continuity equation there are four unknowns: velocity u on the direction of x, velocity v on the direction of y, velocity w on the direction of z, and pressure p.

2.1.3. Reynolds-Averaged-Naviar-Stokes (RANS) Equation

In the present works[10], the RANS simulations are performed in the $k-\epsilon$ turbulence model, where the turbulent kinetic energy and turbulent dissipation equation are solved:

$$\frac{\partial}{\partial t}(\rho k)+\frac{\partial}{\partial x_i}(\rho k u_j)=\frac{\partial}{\partial x_j}\left[\left(\mu+\frac{\mu_t}{\sigma_k}\right)\frac{\partial k}{\partial x_j}\right]+G_k-\rho\epsilon-Y_M+S_k \tag{10}$$

$$\frac{\partial}{\partial t}(\rho \epsilon)+\frac{\partial}{\partial x_j}(\rho k u_j)=\frac{\partial}{\partial x_j}\left[\left(\mu+\frac{\mu_t}{\sigma_\epsilon}\right)\frac{\partial \epsilon}{\partial x_j}\right]+\rho C_1 S_\epsilon-\rho C_2\frac{\epsilon^2}{k+\sqrt{v\epsilon}}+S_\epsilon \tag{11}$$

where $\eta=S\frac{k}{\epsilon}, S=\sqrt{2S_{ij}S_{ij}}; k$ is the turbulent dissipation; G_k indicates the generation of turbulence kinetic energy produced by the mean velocity gradients; Y_M denotes the contribution of fluctuation dilatation in compressible turbulence to the overall dissipation rate; C_2 and C_3 are constants; σ_k and σ_ϵ are the turbulent Prandtl number for k and ϵ, respectively; S_k and S_ϵ are source terms.

2.2. Geometry, computational domain and boundary conditions

2.2.1. Geometry

This paper uses Solidworks as a tool to design 3D model of the vehicle, which subsequently undergoes computational fluid dynamics simulation, done by the Solidworks Flow Simulation. In general, the model in this paper is mainly composed of three parts: cabin, body, and tire. All the above structures are created by surface extrudes, which is a fundamental tool in Solidworks that stretches a two-dimensional face into threedimensional body, as shown in Figure 2:

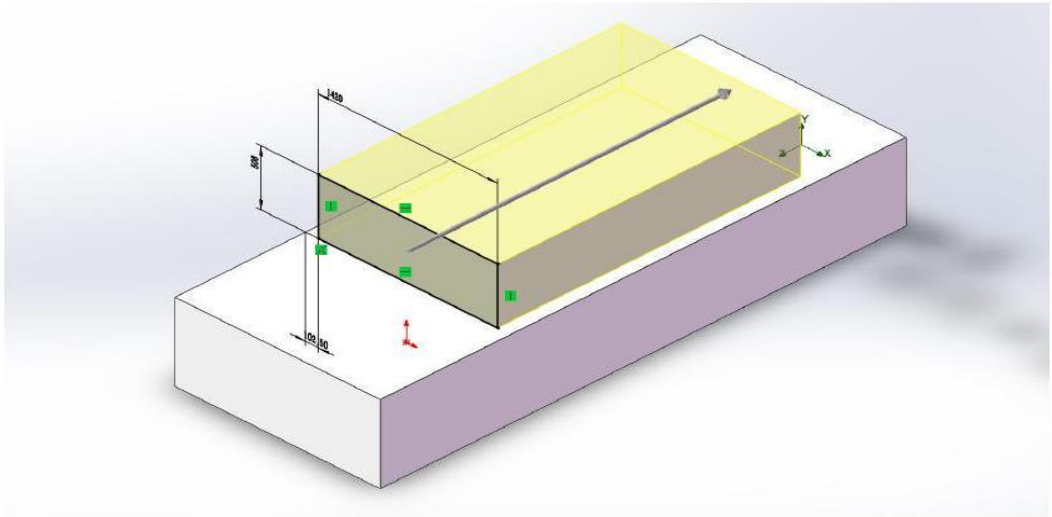


Figure 2: Using surface extrudes to create the cabin

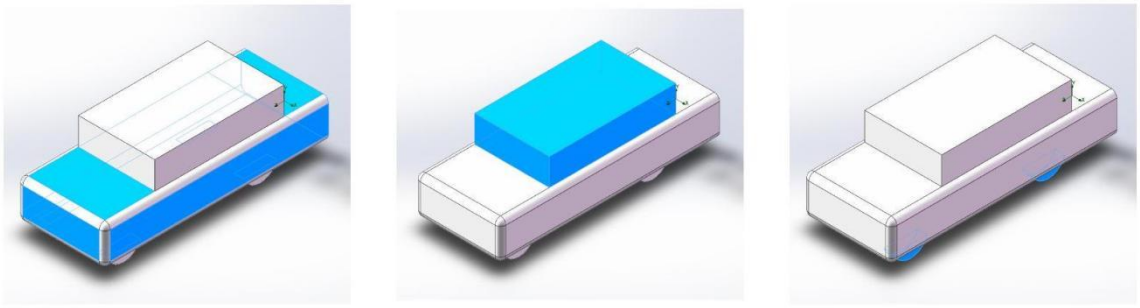


Figure 3: Modeling of cabin, body, and tires

where the length of the vehicle model is set to 4165 mm, the width to 1625 mm, the height to 1438.5 mm, the tire width and variable length to 180 mm and 325 mm respectively. With the basic model being designed, four design parameters are then adjusted to different value in order to optimize the vehicle's aerodynamic performance, especially on drag coefficient, which is quantified by the simulation. Those parameters are:

Angle of the front window, $\alpha(^\circ)$
Angle of the hood, $\beta(^\circ)$
Angle of the back window, $\theta(^\circ)$
Length of the trunk, $L_t(mm)$

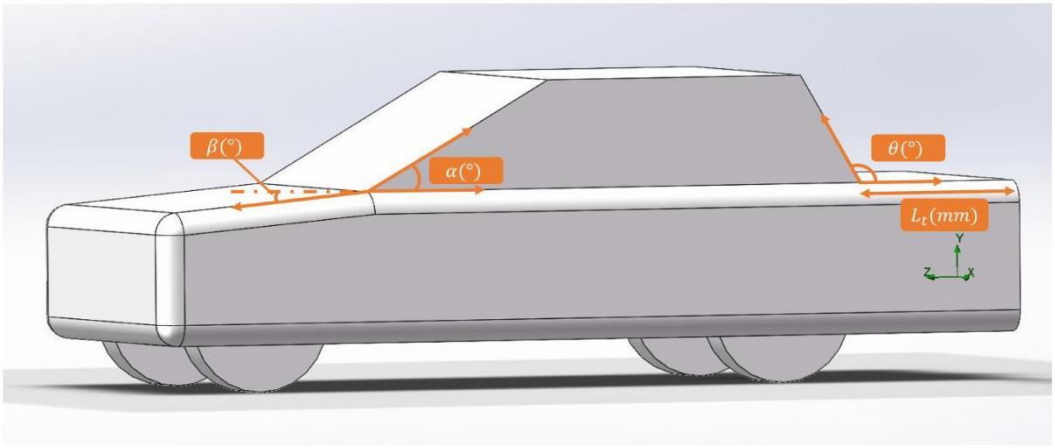


Figure 4: Demonstration of four design parameters

Table 1: DoE parameters to be tested

Angle of the front window	Angle of the hood	Angle of the back window	Length of the trunk
90°	10°	150°	1320 mm
60°	5°	120°	660 mm
30°	0°	90°	0 mm

Table 1 labels the values in each of the design parameters that will be simulated. To carry out the simulation that is achievable in limited time under limited computer performance but with the highest accuracy as possible, design of experiment (DoE) is adopted, which will be explicated in Section 3.

2.2.2. Computational domain and boundary conditions

This paper utilizes the flow simulation tool in Solidworks to conduct numerical simulations on a threedimensional model. In the initial setup, the "Wizard" option is selected to create a new Flow Simulation project. Then, the physical characteristics are defined. In this study, thermal conduction within solids and transient analysis are disabled to reduce computational complexity. Additionally, factors such as humidity and surface roughness of the model are neglected. Gravity is considered, and the fluid is assumed to be air with both laminar and turbulent flow. For the environmental conditions, the gauge pressure is set to 101325.00 Pa, and the velocity parameter is chosen to reflect the real-world scenario of a car traveling at a speed of 60 kilometers per hour, which corresponds to an air velocity of 16.67 meters per second in the opposite direction.

Once the model is established, the next step is to select a computational domain that is not adjacent to the model's surfaces. Due to the significant impact of the car's wake current on its aerodynamic performance and its existence over a long distance behind the car, a substantial length is chosen for the rear part of the car to better simulate the wake. Similarly, to replicate the car's driving state, distances greater than several times the car's length are selected for the front, top, and side of the car. It is worth noting that when the computational domain reaches a certain size, the flow field around the car is no longer constrained by the domain size. To be specific, the chosen computational domain in this study is as follows: $5L$ in front of the vehicle, $8L$ in the back of the vehicle, $3L$ on the two sides, $3L$ on the top, and 0 at the bottom, referring to the surface that the vehicle is driving on (equals one unit length of the vehicle).

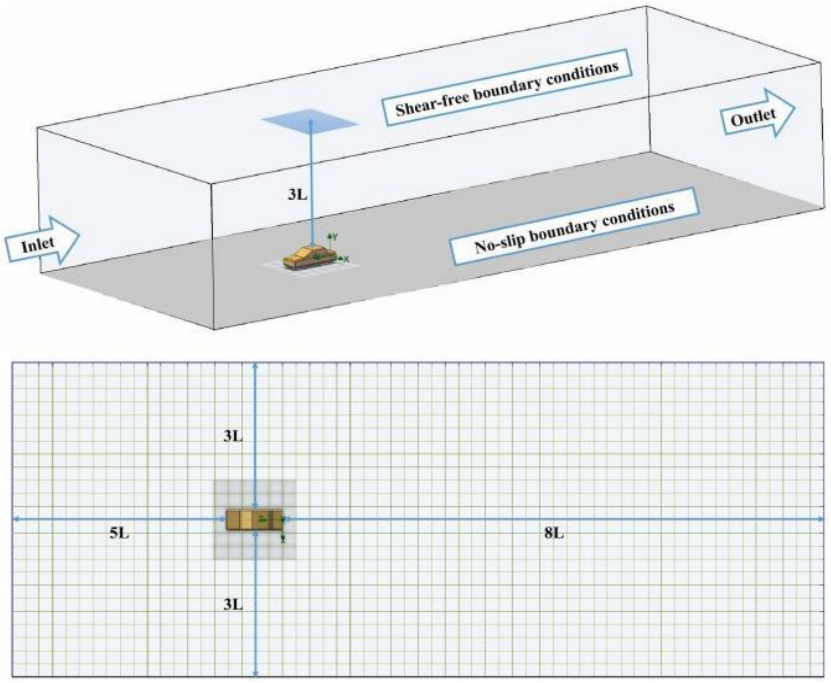


Figure 5: Schematic of computational domain and boundary conditions

After the computational domain is set, the boundary conditions are needed to be imposed. The velocity inlet boundary condition is applied on the inlet, and the pressure-outlet boundary is imposed on the outlet. The surfaces of the car and the ground are set as no-slip boundary conditions, and while the side and top walls are treated as free-slip boundaries.

2.3. Mesh generation and grid independence study

The mesh generation process creates grids that discretize the computational domain, and, in each limited three-dimensional space, the calculation of drag force exerted by air is then performed. When the calculation network is generated, the denser the grid division, the better the accuracy of the simulation results, but at the same time, longer duration for calculation is taken and larger CPU space is occupied.

To make more accurate measurement, it is also important to increase the density of the grids that discretize the space near the vehicle model, so that pivotal factors of a vehicle's aerodynamic performance such as turbulence, separation, and reattachment can be better captured.

Before starting simulation, it has to be clarified how the final mesh is chosen so that it guarantees a acceptable duration of calculation while making sure that the results of other choices do not differ significantly. This paper considers the average drag coefficient C_d, lift coefficient C_l, and the recirculation region (See Fig.7) as critical quantities that determine whether the mesh is good enough. Hence, a grid independence study is performed, which takes into account critical simulation results and compares them with the number of grids. We take the vehicle with $\alpha = 45°, \beta = 2.5°, \theta = 90°$, and $L_t = 0$ mm (shown in Fig.6) as an example to perform the grid independence study. Three sets of grids, i.e., Coarse grid, Standard grid, and Fine grid, with different resolutions are considered. Table 2 summarizes the grid information and the corresponding results for the three sets of grids.

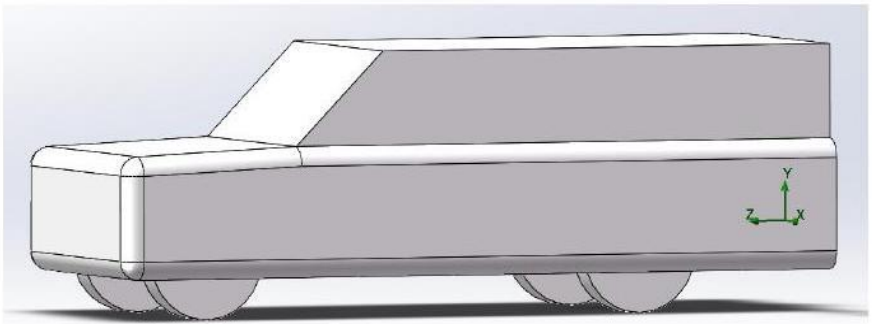


Figure 6: Vehicle model used in the grid independence study, with its design parameters labeled in the table above

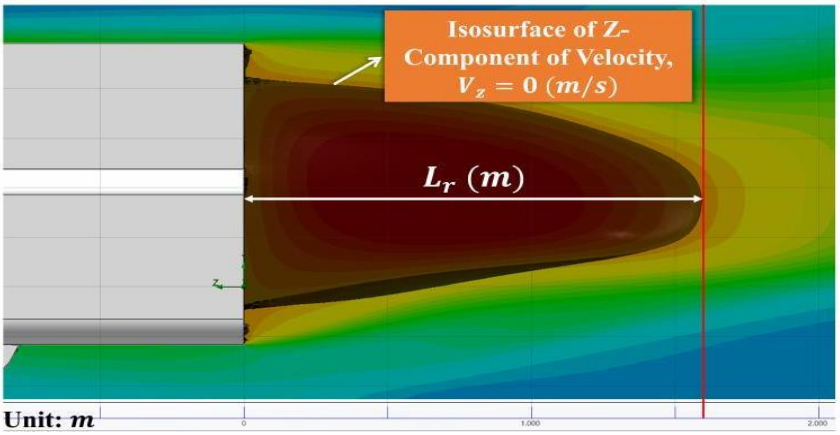


Figure 7: Method to identify the recirculation region, which is then standardized by dividing the vehicle length $L = 4165$ mm

Table 2: Grid independence study, where three grids are tested

Grid	Number of Grid Cells	$\bar{C_d}$	$\bar{C_l}$	Recirculation region, L_r
Coarse	1,096,829	0.3801155	0.4556919	$0.3649L$
Standard	3,147,902	0.3616437	0.4506147	$0.3854L$
Fine	5,629,822	0.3591843	0.4566344	$0.3890L$

As can be seen from Table 2, the gap between Standard and Fine grid is approximately 2.5 million cells. while both the simulated drag coefficient $\bar{C_d}$ and recirculation region L_r change in less than 1 percent, which are satisfactorily close to an accurate result. Therefore, the Standard Grid with roughly 3.1 million cells will be chosen and applied in later works, as shown in Figure 8.

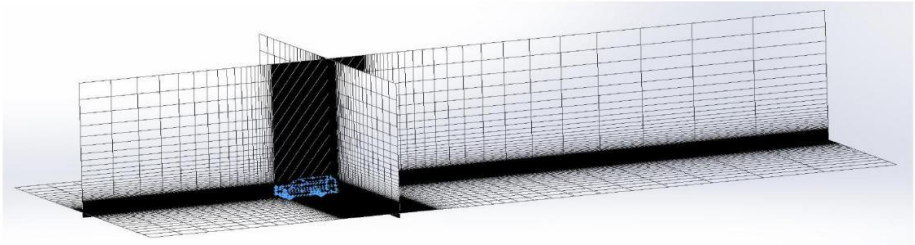


Figure 8: A bird's eye view of the final chosen meshing method with approximately 3.1 million grid cells, the vehicle model is highlighted in blue

2.4. Drag force and coefficient

Aerodynamic drag is essentially the forces exerted on the object while it's interacting with the air flow. Normally, two types of stresses are exerted on the object: tangential wall shear stress τ_W due to viscosity and stress due to pressure P, which are also called viscous drag and pressure drag. Pressure drag is the greatest contributor to a vehicle's aerodynamic drag, accounting for approximately 50% to 65%. It mainly arises from the pressure difference found around the vehicle due to the presence of flow separation and recirculation region behind the vehicle.

Drag coefficient is a dimensionless quantity in fluid dynamics that represents the resistance of an object in a fluid. A smaller drag coefficient indicates the object has less fluid resistance, and it's determined by the shape and surface characteristics of the object [11]. To compute the drag coefficient of each model, equation 12 is inputted into the simulator as Equation Goal, deriving drag coefficient C_d from the dependent variable F_d, which is determined during the simulation.

$$\begin{aligned} C_d &= \frac{2F_d}{\rho u^2 A} \\ &= \frac{2\times F_d}{1.225(\ \mathrm{kg/m^3})\times 16.67(\ \mathrm{m/s^2})^2\times 1.919(\ \mathrm{m^2})} \\ &= 0.051(\ \mathrm{N^{-1}})\times F_d \end{aligned} \tag{12}$$

Where F_d refers to drag, ρ refers to air density, u represents the velocity of an object relative to air, and A represents the the effective cross-sectional area.

2.5. CAD and CFD software

At the beginning of auto body modeling, appropriate software should be selected first, which not only meets the requirements of auto body modeling, but also meets the requirements of efficiency, convenience and accuracy [12].

This paper uses SOLIDWORKS, which is one of the most popular automotive design softwares developed by Dassault Systemes S.A. Considering the requirements for accuracy and flexibility in body modeling, SOLIDWORKS' powerful 3D modeling capabilities are brought into play. These include building from two-dimensional planes to three-dimensional models, while providing features such as rounded corners/edges, shell extraction, die drawing, and mirroring to greatly reduce modeling difficulty and improve the modeler's efficiency. SOLIDWORKS can theoretically build any three-dimensional model imaginable.

Another reason for choosing SOLIDWORKS for this paper is its robust built-in applications, including flow simulation, which will be used in this article. SOLIDWORKS also provides convenient and intuitive data visualization, including section diagrams, surface diagrams, isosurfaces, flow tracks, particle studies, etc., to help this paper clearly display experimental results and draw conclusions.

3. Design of Experiment (DoE)

Utilizing the principles of Design of Experiments (DoE), one can analyze the distinct and interrelated impacts of various factors affecting the outcomes of measurements. Additionally, DoE

serves as a valuable tool for acquiring insights and approximating optimal operational conditions within a system, process, or product.

The versatility of DoE extends to diverse investigation goals, with particular significance during initial screening inquiries to ascertain the most influential factors. Subsequently, it aids in the optimization process, offering enhanced comprehension of how these critical, controllable factors influence responses and vital quality attributes.

Moreover, DoE finds a crucial application in enhancing production efficiency by pinpointing factors capable of reducing resource consumption, minimizing costs, and reducing wait times. It also plays a pivotal role in conducting robustness tests, ensuring product or system quality prior to market release.

3.1. Principle and implementation of DoE

An experiment examines the effects of different factors to the results and sometimes aims to determine the specific factor levels that optimize the results. When the experiment has to take into account more than three factors, it will be relatively time-consuming and demanding to perform a full-factorial design. On the other hand, if we compromise the number of experiments for efficiency without careful selection, the result computed from the combination of factor levels might not be representative of each factors' performance.

The Design of Experiment, in contrast, selects representative, or balanced, factor level combinations and omits the combination that will convey the same information through The Yates Algorithm, which generates the typical Design of Experiment (DoE) matrix:

Table 3: A $L_8(2^7)$ DoE matrix

Trials	A	B	C	D	E	F	G
1	1	1	1	1	1	1	1
2	1	1	1	2	2	2	2
3	1	2	2	1	1	2	2
4	1	2	2	2	2	1	1
5	2	1	2	1	2	1	2
6	2	1	2	2	1	2	1
7	2	2	1	1	2	2	1
8	2	2	1	2	1	1	2

Table 4: A $L_9(3^4)$ DoE matrix

Trials	A	B	C	D
1	1	1	1	1
2	1	2	2	2
3	1	3	3	3
4	2	1	2	3
5	2	2	3	1
6	2	3	1	2
7	3	1	3	2
8	3	2	1	3
9	3	3	2	1

where, in the case of Figure $3, L_8$ denotes the number of trials that are performed in the experiment; 2^7 refers to seven factors, and each has a factor level of two. As can be observed from the above examples, the levels in a specific factor have the same number of appearance (in each row, the number $1,2,3$ ... have the same frequency); in any two rows, the horizontal number pairs $(1,1), (1,2), (1,3), (2,1), (2,2), (2,3), (3,1), (3,2), (3,3)$ also appear in the same frequency. These combined properties render the DoE matrix orthogonality, making the experimental trials representative and balanced.

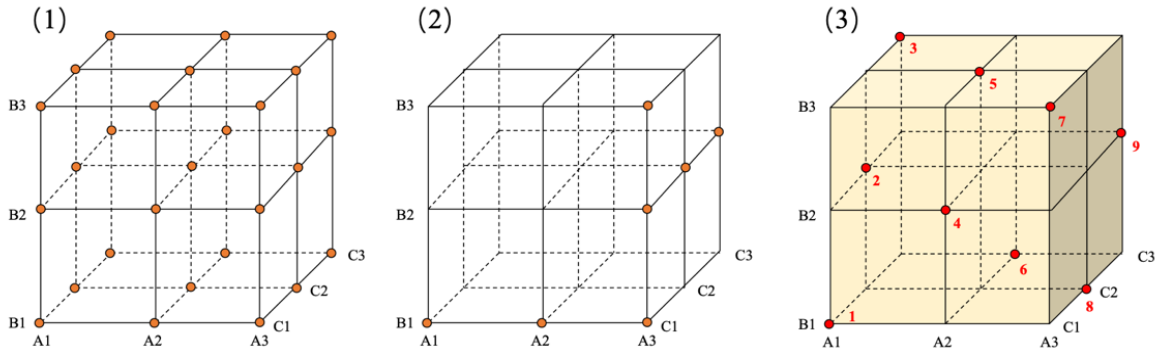


Figure 9: A visualized comparison between (1) full-factorial design, (2) simple design, and (3) DoE

Figure 9 takes design $L_9(3^3)$ as an example. It can be seen that all six faces have three data points (the trials), and each line is occupied by one point, again proving that DoE selects balanced and representative data points.

In this paper, four design parameters are considered in Section 2.2.1, and each comprises three specific value to be simulated, making the number of factors to be four, and number of factor levels to be three. Hence, DoE matrix $L_9(4^3)$ is applied, with its value specified below:

Table 5: The DoE matrix used in this article, which pinpoints nine different trials to be performed in the experiment and leaves the blank of the output- C_d to be filled after the numerical simulation

Trials	$\alpha(^\circ)$	$\beta(^\circ)$	$\theta(^\circ)$	L_t(mm)	Output- C_d
1	1(30)	1(0)	1(90)	1(0)	
2	1	2(5)	2(120)	2(660)	
3	1	3(10)	3(150)	3(1320)	
4	2(60)	1	2	3	
5	2	2	3	1	
6	2	3	1	2	
7	3(90)	1	3	2	
8	3	2	1	3	
8	3	3	2	1	

3.2. Analysis of a *DoE*

As mentioned earlier, Design of Experiment help reducing workload, finding the optimized combination, and quantifying the most influential factors. The following flow chart illustrates the process of results analysis in a DoE:

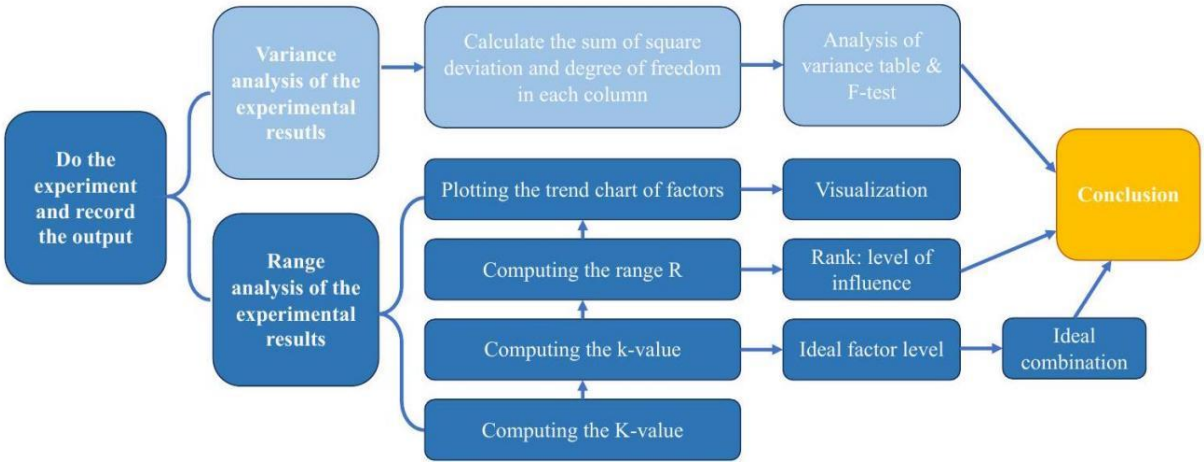


Figure 10: A flow chart of the DoE analysis, this article adopts the range analysis, which is highlighted in dark blue color

To elaborate, we will take a $L_9(4^3)$ DoE matrix (which is same one as this article will use) as an example. The first step to perform a DoE range analysis is to calculate the K-value, who's results form a matrix with the size "factor level $\times$ number of factor":

$$\boldsymbol{K} = \begin{bmatrix} K_{1A} & K_{1B} & K_{1C} & K_{1D} \\ K_{2A} & K_{2B} & K_{2C} & K_{2D} \\ K_{3A} & K_{3B} & K_{3C} & K_{3D} \end{bmatrix} \tag{13}$$

where K_{1A}, K_{2A} or K_{3A} represent the sum of the result from factor A, level 1, 2 or 3.

Trials	$\alpha(°)$	$\beta(°)$	$\theta(°)$	$L_t(mm)$	Output-C_d
1	1 (30)	1 (0)	1 (90)	1 (0)	C_{d1}
2	1	2 (5)	2 (120)	2 (660)	C_{d2}
3	1	3 (10)	3 (150)	3 (1320)	C_{d3}
4	2 (60)	1	2	3	C_{d4}
5	2	2	3	1	C_{d5}
6	2	3	1	2	C_{d6}
7	3 (90)	1	3	2	C_{d7}
8	3	2	1	3	C_{d8}
8	3	3	2	1	C_{d9}

$$\begin{cases} K_{1A} = C_{d1} + C_{d2} + C_{d3} \\ K_{2A} = C_{d4} + C_{d5} + C_{d6} \\ K_{3A} = C_{d7} + C_{d8} + C_{d9} \\ K_{1B} = C_{d1} + C_{d4} + C_{d7} \\ \vdots = \vdots + \vdots + \vdots \\ K_{2D} = C_{d2} + C_{d6} + C_{d7} \\ K_{3D} = C_{d3} + C_{d4} + C_{d8} \end{cases}$$

Figure 11: A demonstration of the computation of K-values, an instance of K_{1B} is highlighted in the blue color

An averaged K-value k is then calculated in order to make direct comparison and elicit the best combination of factor level:

$$\boldsymbol{k} = \frac{\boldsymbol{K_{i\times j}}}{i} \tag{14}$$

Where i is the factor level, j is the number of factors. In terms of this paper's problem, $\boldsymbol{k} = \boldsymbol{K}/3$.

According to the traits of an orthogonal test (DoE), the experiment conditions for A_1, A_2, and A_3 are the same. Thus, if factor A has not influence on the results, then theoretically k_{1A}, k_{2A}, and k_{3A} should be the same. In contrary, if they are unequal, factor A does have its own impact on the result. By looking for the maximum (or minimum, depending on the context of experiment) k-value for each factor, an optimized combination can be elicited, as in each factor, its factor level achieves the best k-value.

In terms of the level of influence from each factor, a new concept-range-has to be introduced. As mentioned earlier, factor A does have influence if k_{1A}, k_{2A}, and k_{3A} are unequal; the difference between them, further on, should measure their level of impact. The range R, a measurement of the

influence level of each factor, thus quantifies the difference between maximum and minimum value among k_{1A}, k_{2A}, and k_{3A} :

$$R = \max\{k_1, k_2, k_3 \cdots\} - \min\{k_1, k_2, k_3 \cdots\} \quad (15)$$

Hence, if a design parameter has the highest range R, it means that it is the most influential factor to the results, and vice versa.

4. Results and Discussion

4.1. The DoE analysis

After the initial setup was completed, this paper conducted calculations for each trial of numerical simulations mentioned earlier. Upon completion of result loading, this paper further analyzed each set of models by exporting the results (averages) of the target equation and visualizing the aerodynamic performance of the vehicles.

Trials	$\alpha(°)$	$\beta(°)$	$\theta(°)$	$L_t(mm)$	Output-C_d
1	1 (30)	1 (0)	1 (90)	1 (0)	0.3297859
2	1	2 (5)	2 (120)	2 (660)	0.4273782
3	1	3 (10)	3 (150)	3 (1320)	0.4492890
4	2 (60)	1	2	3	0.4923088
5	2	2	3	1	0.5079619
6	2	3	1	2	0.5004923
7	3 (90)	1	3	2	0.4981847
8	3	2	1	3	0.5494221
8	3	3	2	1	0.5790989

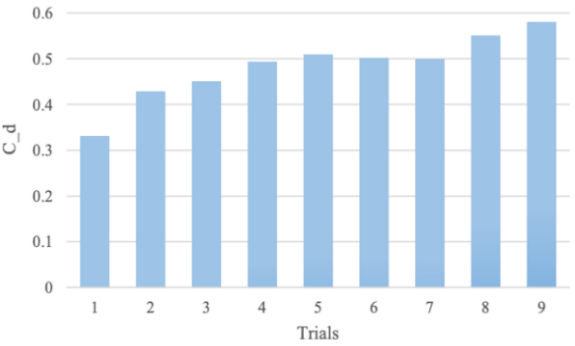


Figure 12: Result of numerical simulations of the nine trials based on DoE

Referring to Figure 11 and Equation 14, the $\boldsymbol{K}$ and $\boldsymbol{k}$ matrix of these DoE outputs can then be calculated and further analyzed:

$$\boldsymbol{K} = \begin{bmatrix} 1.2064531 & 1.3202794 & 1.3797003 & 1.4168467 \\ 1.500763 & 1.4847622 & 1.4987859 & 1.4260552 \\ 1.6267057 & 1.5288802 & 1.4554356 & 1.4910199 \end{bmatrix} \quad (16)$$

$$\boldsymbol{k} = \begin{bmatrix} 0.4022 & 0.4401 & 0.4599 & 0.4723 \\ 0.5003 & 0.4949 & 0.5000 & 0.4754 \\ 0.5422 & 0.5096 & 0.4851 & 0.4970 \end{bmatrix} \quad (17)$$

From Equation 17 we can see that k_{1A}, k_{1B}, k_{1C}, and k_{1D} are the minimum value for each design parameter (which indicates a good performance). Hence, an optimal design from this Design of Experiment can be selected: $A_1B_1C_1D_1$, corresponding to a $30°$ front window, $0°$ hood, $90°$ back window, and no trunk.

Additionally, it can also be seen that, for each design parameter, its three k-value differentiates with another, indicating that all four design parameters have certain influences on the vehicle's overall aerodynamic performance. To measure the extent, an array of the k-value range of each parameter is calculated, based on Equation 15:

$$\boldsymbol{R} = \{0.1400, 0.0695, 0.0401, 0.0247\} \quad (18)$$

Where we can see that parameter A, or the angle of the front window, has the greatest impact on the vehicle's aerodynamic drag with the largest range-0.14. In contrast, design parameter D, or the length of the trunk, has the lowest impact. The level of influence (from high to low) is $ABCD$.

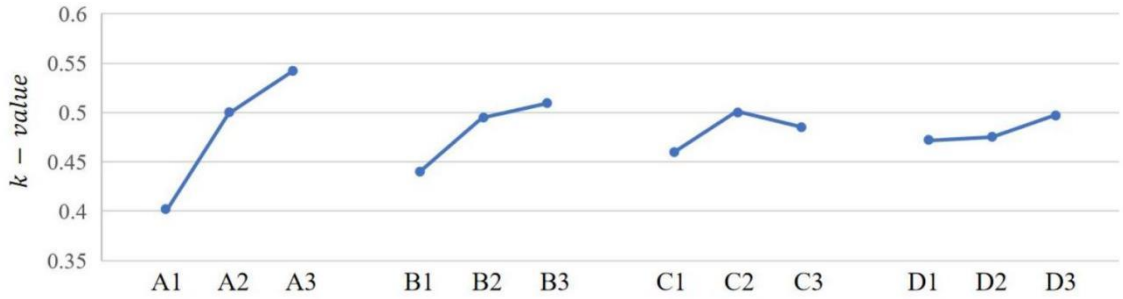


Figure 13: Trend line of the k-value in each design parameter

Through the DoE analysis above and the trend line of the k-value in Figure 13, one can conclude that the most significant factor on the vehicle aerodynamics is the angle of the front window. And the angles of the hood/back window can also affect the vehicle aerodynamics. The length of the trunk, on the other hand has the smallest influence. Therefore, the following sections will focus on design parameters A and B-angle of the

front window and the hood-and closely examine their influences on vehicle aerodynamics from the recorded and visualized data.

4.2. Vehicle Aerodynamic analysis

In this section, the effects of the primary factors of the vehicle geometry model on its aerodynamics are then carefully examined. Meanwhile, new models are also constructed and gone through similar numerical simulation, providing more data points available for analyzing and trend discovering.

4.2.1. Effect of the angle of the front window

Apart from incorporating two more front window angle, this section also holds the other design parameters constant, so that a direct influence solely from the angle of the front window can be observed. The parameters of the five models explicated in this section can be seen in Table 6.

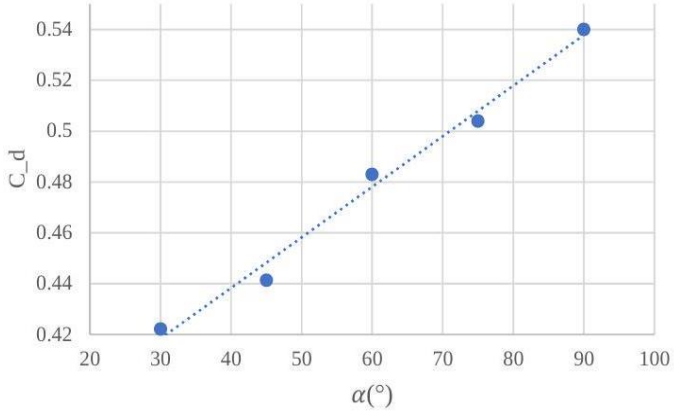


Figure 14: Effects on drag coefficient

Table 6: The five vehicle models

	$\alpha(^\circ)$	$\beta(^\circ)$	$\theta(^\circ)$	$L_t(mm)$
1	30	0	90	660
2	45	0	90	660
3	60	0	90	660
4	75	0	90	660
5	90	0	90	660

From Figure 14, it can be observed that the overall drag coefficient of the vehicle increases with an increase in the angle of front window, exhibiting an approximate linear growth. At the lowest point of 30°, the drag coefficient of the vehicle is approximately 0.42 , while it reaches around 0.54 at a front windshield angle of 90°.

To further understand the trends of the drag coefficients with the angle of front window and the underlying principles behind them, this paper will proceed to examine Cut Plots and Surface Plots, among other visualizations, and discuss them accordingly.

From Figure 15 the velocity cut plot, it can be observed that as the angle of the front window increases, flow separation and the formation of the wake vortex become more pronounced. This is caused by the convergence of the airflow coming from the upper surface and the outflow from the bottom. The formation and dissipation of large-scale vortices lead to an increase in energy consumption of the airflow, resulting in a significant increase in aerodynamic drag [14]. At an angle of 90°, flow separation already begins on the upper side of the front window, while at an angle of 30°, flow separation is significantly delayed. This reduces the size of the low-pressure area behind the car, thereby decreasing the pressure drag. Additionally, as the angle increases, the pressure on the front of the car increases. This is because the windshield angle becomes increasingly vertical, resulting in less pressure being distributed in the horizontal direction, which leads to drag force. In summary, increasing the angle not only increases the horizontal component of the pressure on the front of the car but also makes flow separation more pronounced, reducing the pressure behind the vehicle. The combined effect of these factors contributes to the observed trend shown in Figure 14.

In Figure 16, when comparing the Flow Trajectory (color representing velocity) and the pressure distribution on the front window at angles of 90° and 30°, it can be observed that the flow velocity behind the car is significantly slower and the vortices are more concentrated at a front window angle of 90°. Furthermore, the pressure on the front window is higher and has no vertical component in the case of a 90° angle.

It is important to note that when creating Cut Plots, Surface Plots, and Flow Trajectory, it is crucial to use consistent units, including the same upper and lower limits and consistent color bars. This helps avoid visualization errors or misleading experimental information, and ensures rigorous experimental conclusions.

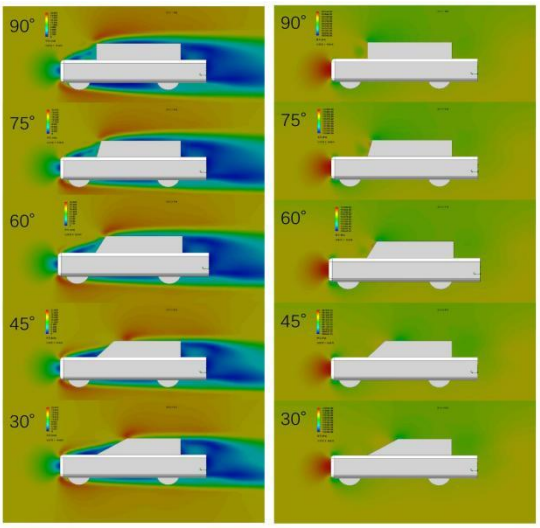


Figure 15: Effects of the angle of front window on velocity and pressure

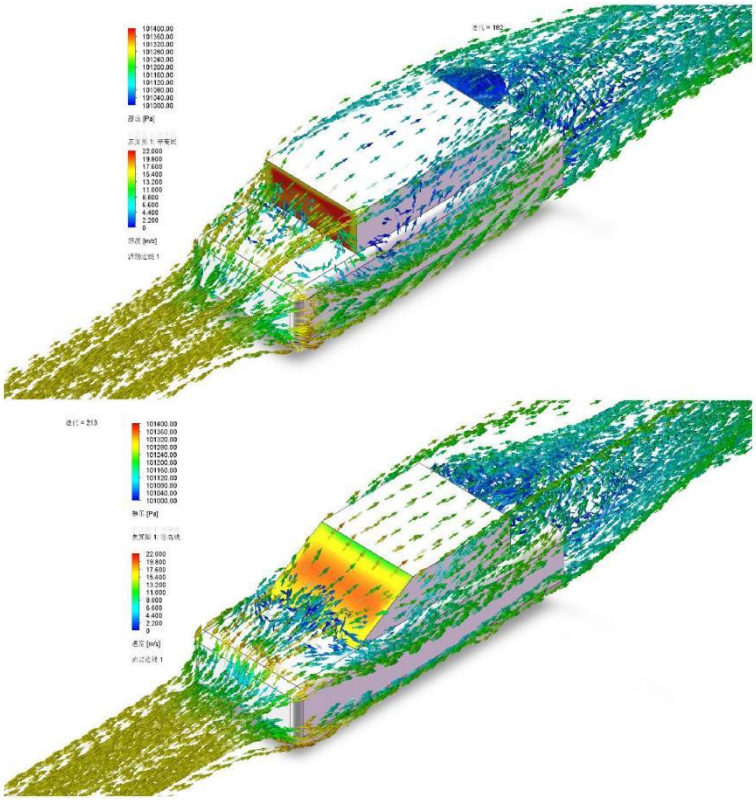


Figure 16: Effects of the angle of front window on Flow Trajectory

By comparing the results, it can be observed that adjusting the angle of the front window to 30°, compared to the 90° model, significantly reduces the drag coefficient by 22.2%.

4.2.2. Effect of the angle of the hood

Referring back to the result of DoE, another influential design parameter is the angle of the hood. In the previous analysis, the study optimized the angle of the front window from 90° to 30°, effectively reducing both drag and lift coefficients. However, upon examining Figure 18, it is evident that there is still significant separation and reattachment of the airflow at the rear edge of the hood, accompanied by dense clockwise vortices. This phenomenon occurs because the pressure in this region is higher compared to the front edge of the hood and the upper surface. Consequently, this not only increases aerodynamic drag but also leads to the accumulation of dust, leaves, and other debris on the windows.

These issues indicate the need for further investigation and optimization. Potential approaches may involve modifying the design of the hood or introducing additional airflow control measures to mitigate flow separation and reattachment. Additionally, considering other aerodynamic enhancements, such as the implementation of spoilers or reducing the side surface area of the vehicle, could also be beneficial.

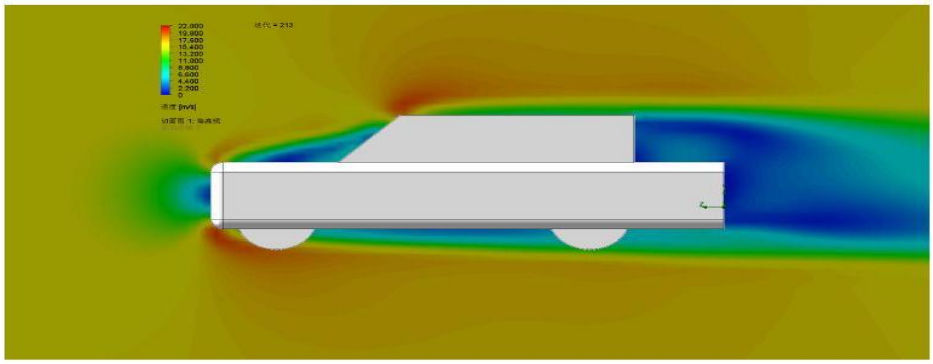


Figure 17: Cut Plot of air velocity when $\theta = 45°$

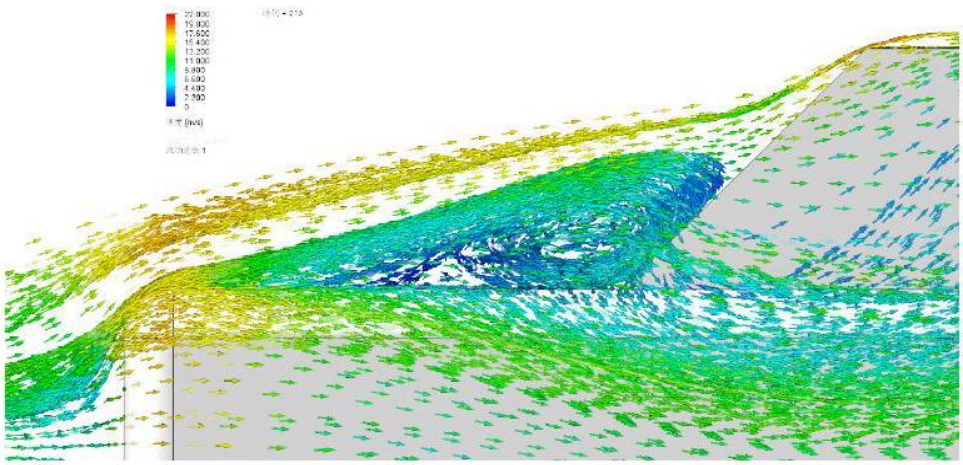


Figure 18: Flow Trajectory when $\theta = 45°$

Taking into account real-world considerations, the next step is to conduct numerical simulations and analyze the results for five different downward angles of the hood: $0°, 2.5°, 5°, 7.5°$, and $10°$, as can be seen from table 7 . By observing Figure 19, it can be noticed that adjusting the angle of the front hood to $2.5°$ results in a significant reduction in the drag coefficient of the model, decreasing from the original value of 0.44 to approximately 0.419 . As the angle β continue to increases, the drag coefficient then increases to around 0.425 .

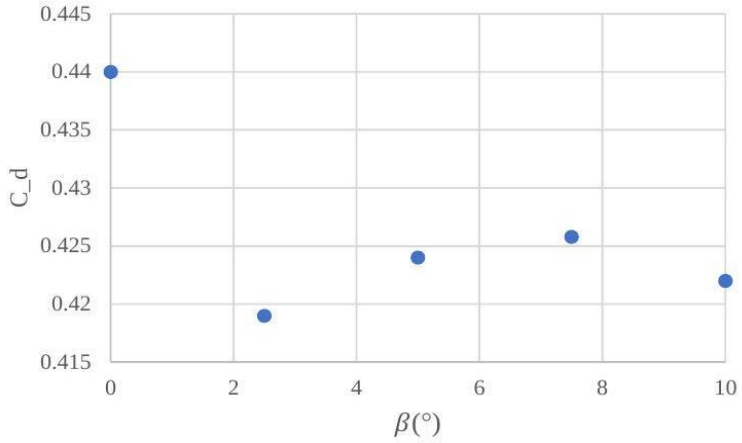


Figure 19: Effects on drag coefficient

	$\alpha(°)$	$\beta(°)$	$\theta(°)$	L_t(mm)
1	45	0	90	660
2	45	2.5	90	660
3	45	5	90	660
4	45	7.5	90	660
5	45	10	90	660

Table 7: The five vehicle models

From Figure 20, it can be observed that although changing the angle of the hood can reduce the turbulence around the hood and front window, this adjustment also affects the overall aerodynamic performance of the vehicle. At an angle of $2.5°$, the airflow around the front hood and front window

is the fastest compared to the other three cases. According to Bernoulli's principle, as the airflow velocity increases, the total pressure energy or potential energy of the fluid decreases, resulting in a decrease in the pressure exerted on the front of the vehicle. Additionally, at angles of $7.5°$ and $10°$, there is significant separation of the airflow from the bottom of the vehicle, leading to more pronounced separation and low-pressure area at the rear of the vehicle. In the rear of the vehicle, although the airflow is relatively slower, it becomes irregular, rendering Bernoulli's principle no longer applicable. In summary, adjusting the front hood angle to $2.5°$ results in a smaller pressure difference between the front and rear of the vehicle compared to other cases, thereby achieving an optimized drag coefficient.

However, such result is unexpected if we refer back to the DoE results Table 12, which documents that $\beta = 0°$ should be the optimized design. The reason can be the choice of factor level while preparing for the DoE, where $\beta = 0°, \beta = 5°$, and $\beta = 10°$ are chosen, rendering $\beta = 2.5°$ being untested.

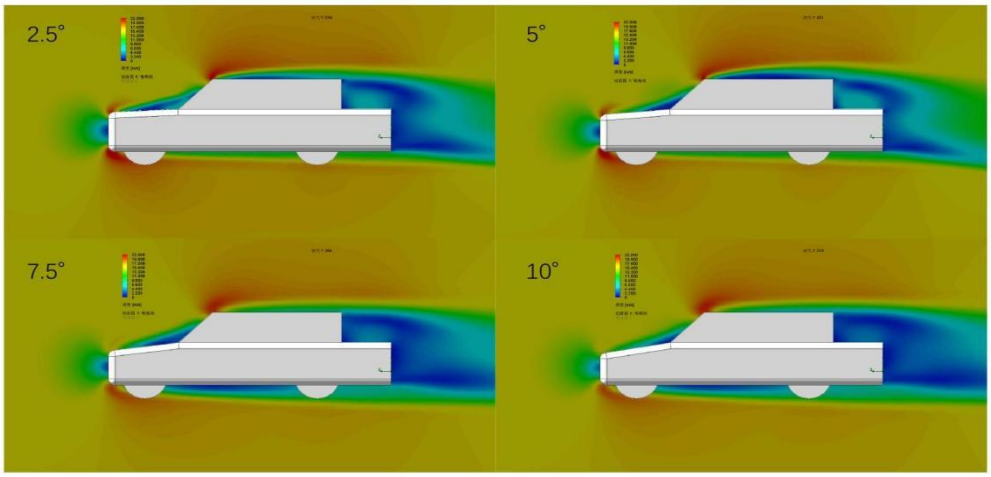


Figure 20: Effects of the front hood angle on air velocity

4.2.3. Composition of drag forces

As mentioned earlier, if only external air flow is considered, the aerodynamic drag is consisted of only pressure drag and frictional drag. Their ratio, however, can vary significantly across different vehicle model.

Table 8: The ratio of pressure drag and friction drag of the nine trials in DoE, where C_{dp} refers to drag coefficient due to pressure, and C_{dv} refers to drag coefficient due to viscosity

	Drag (Z)	Pressure Drag (Z)	Friction Drag (Z)	C_d	C_{dp}	C_{dv}	C_{dp}/C_{dv}	C_{dp}/C_d	C_{dv}/C_d
1	$107.714N$	$98.537N$	$9.178N$	0.3298	0.3017	0.0281	10.74	91.48%	8.521%
2	$139.590N$	$129.568N$	$10.022N$	0.4274	0.3967	0.0307	12.93	92.82%	7.180%
3	$146.746N$	$138.095N$	$8.651N$	0.4493	0.4228	0.0265	15.96	94.10%	5.895%
4	$160.798N$	$155.201N$	$5.597N$	0.4923	0.4752	0.0171	27.73	96.52%	3.481%
5	$165.91N$	$158.782N$	$7.128N$	0.5080	0.4861	0.0218	22.28	95.70%	4.296%
6	$163.47N$	$156.704N$	$6.766N$	0.5005	0.4798	0.0207	23.16	95.86%	4.139%
7	$162.717N$	$157.747N$	$4.969N$	0.4982	0.4830	0.0152	31.75	96.95%	3.054%
8	$179.452N$	$174.565N$	$4.887N$	0.5494	0.5345	0.0150	35.72	97.28%	2.723%
9	$189.145N$	$183.671N$	$5.474N$	0.5791	0.5623	0.0168	33.55	97.11%	2.894%

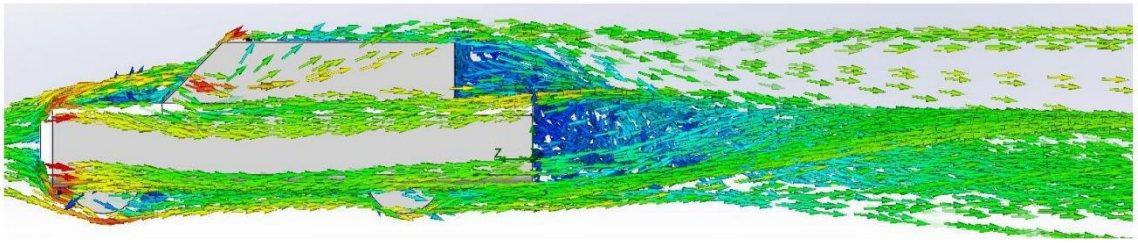


Figure 21: Flow Trajectory when $L_t = 660$ mm

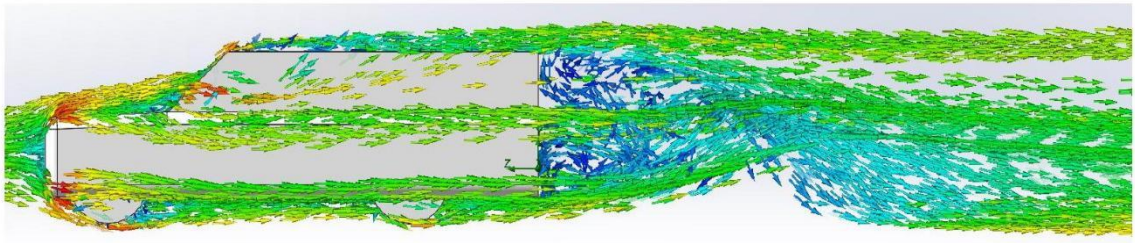


Figure 22: Flow Trajectory when $L_t = 0$ mm

Upon comparing Figures 21 and 22, it is evident that the airflow patterns at the rear of the car model differ significantly due to the variations in the shape of the rear section. When $k = 660$ mm, the presence of a gap at the trunk causes the airflow to separate prematurely from the vehicle's roof. This results in a more chaotic and denser flow of turbulence and vortices behind the vehicle, with relatively fewer undisturbed flow trajectories. In contrast, when $k = 0$ mm, the airflow separation occurs later, and the flow patterns above and below the vehicle are synchronized. This allows the clockwise vortices above and counterclockwise vortices below to converge, without generating more complex and chaotic vortices. By visually comparing the density of the green and blue arrows, it can be observed that the complex vortices at the rear of the car model with $k = 660$ mm lead to a lower pressure, and thus contribute to greater drag difference between the front and the rear, while the airflow at the rear of the car with $k = 0$ mm is relatively more streamlined, resulting in reduced pressure drag.

Referring back to Table 8, it can be seen that models with design parameter $L_t = 0$ mm (Trial 1, Trial 5 , and Trial 9) generally have the greatest C_{dv} than its $L_t = 660$ mm and $L_t = 1320$ mm counterparts, which, again, proves such design reduces the pressure drag at the expense of friction drag by its elongated cabin and roof. The friction drag, however, is also considerably smaller comparing to the pressure drag.

4.2.4. Comparisons between the optimized one and the basic model

To sum up, after using Design of Experiment method and examining two design parameters closely, the optimized design is:

1. Angle of the front window, $\alpha = 30°$
2. Angle of the hood, $\beta = 2.5°$
3. Angle of the back window, $\theta = 90°$
4. Length of the trunk, $L_t = 0$ mm

Such combination of design parameters produces a drag coefficient of 0.3172 , which is 36.9% lower than the basic model with $\alpha = 90°, \beta = 0°, \theta = 90°$, and $L_t = 660$ mm.

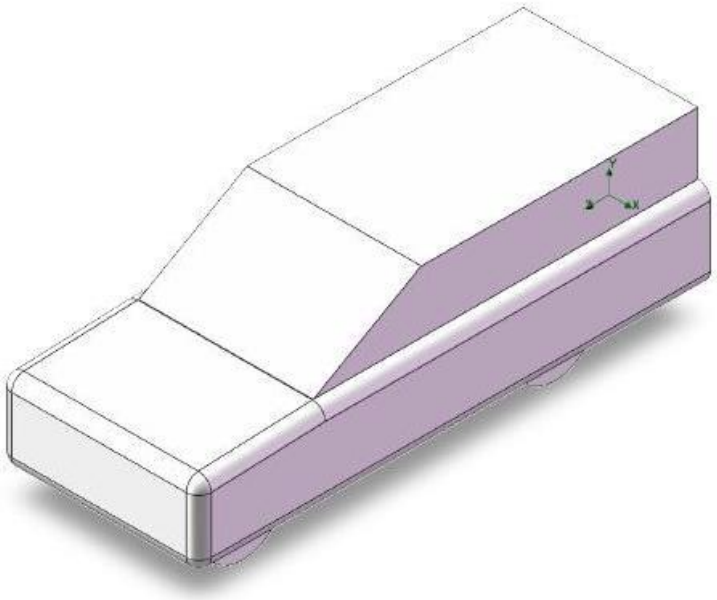


Figure 23: The optimized model

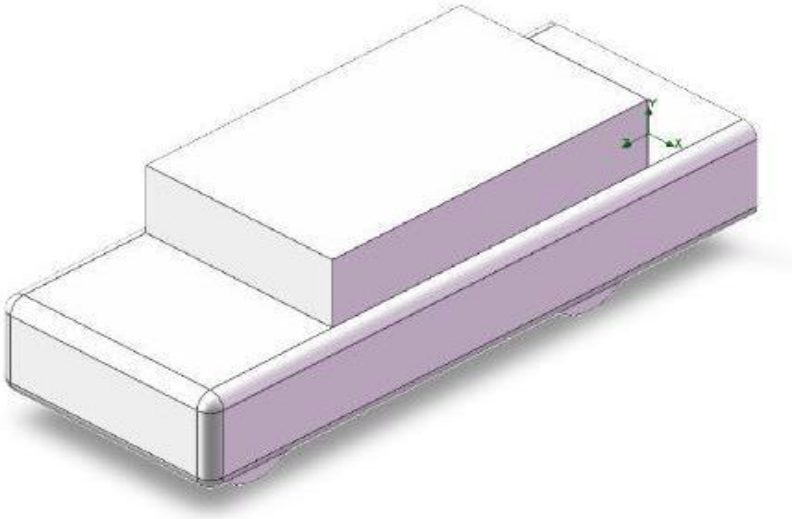


Figure 24: The basic model

5. Conclusion and Further Works

This study optimizes the aerodynamic design of automobiles through the synergistic application of Design of Experiments (DoE) and Computational Fluid Dynamics (CFD). Comparing with the basic model ($\alpha = 90°,\ \beta = 0°, \theta = 90°$, and $L_t = 660$ mm), the optimized model is a wagon car with the four design parameter as follows: $\alpha = 30°, \beta = 2.5°, \theta = 90°$, and $L_t = 0$ mm. The study effectively reduces the drag coefficient of basic model from 0.5025 to the optimized 0.3172 , by approximately 36.9%. Besides, the composition of drag forces of each model is also determined, and this paper has found out that a greater overall drag coefficient normally means a larger C_{dp}/C_{dv} ratio. The successful synergistic application of DoE and CFD proves the applicability of such combination in future works.

There are also important further works after this study to be accomplished. First, the four design parameters of passenger vehicle examined in this study only comprise a little of all the parameters, and might overgeneralize some detailed designs. In the future, a more diverse design parameters

should be researched. Additionally, for the four parameters examined in this study, there are also some flaws. In the Design of Experiment method, only three levels are chosen in each parameters, which might make a even more optimized design been ignored.

References

[1] Cakir, Mustafa. "CFD study on aerodynamic effects of a rear wing/spoiler on a passenger vehicle." (2012).

[2] Guan. Numerical simulation analysis and visualization of automobile flow field. Master's thesis, Dalian University of Technology, 2000.

[3] Huang. Numerical simulation and optimization of vehicle body modeling based on CFD. Master's thesis, Hunan University, 2010.

[4] Du. Automotive aerodynamics. Standards Press of China; 1999.

[5] Shaw. Predicting vehicle aerodynamics using computational fluid dynamics-a user's perspective. SAE Technical Paper; 1988.

[6] Qu, Yu. Optimization on stepping automotive wake structures based on orthogonal test method. *J* Automotive Safety and Energy. 2017; 8(1): p. 59-64. 10.3969/j.issn.1674-8484.2014.00.008

[7] Wu. Active drag reduction mechanism based on MIRA fastback model. Master's thesis, Jilin University, 2018.

[8] Li. Aerodynamic simulation and optimization design of automobile outflow field based on FLUENT. Master's thesis, Lanzhou Jiaotong University, 2014.

[9] Reddy, Gupta. Finding the optimum angle of attack for the front wing of an f1 car using CFD. In: Proceedings of the 4th WSEAS International Conference on Fluid Mechanics and Aerodynamics. Elounda, Greece: [s.n.]; 2006. p. 29-44.

[10] Xu, Shunyuan, and Jiaming Wu. "The maneuverability and hydrodynamics of a tethered underwater vehicle based on adaptive mesh refinement." Ocean Engineering 265 (2022): 112644.

[11] McCormick. Aerodynamics, aeronautics, and flight mechanics. Wiley; 1979.

[12] Su. Numerical simulation of automobile body design and its outflow field. Master's thesis, Dalian University of Technology, 2005.

[13] Zhang, Weng. Numerical simulation of temperature field of air flow field in passenger train. Journal of Computer Science and Technology. 2007; 24(6): p. 904-910.

[14] Ma. Automotive aerodynamics. China Machine Press. 1993.